Effect of Microstructure on the High-Cycle Fatigue Behavior of Ti(43-44)Al4Nb1Mo (TNM) Alloys

Bin Tang [1,*] **, Bin Zhu** [2] **, Weiqing Bi** [1] **, Yan Liu** [1] **and Jinshan Li** [1]

[1]   State Key Laboratory of Solidification Processing, Northwestern Polytechnical University, Xi'an 710072, China; biweiqing@mail.nwpu.edu.cn (W.B.); liuyswallow@163.com (Y.L.); ljsh@nwpu.edu.cn (J.L.)

[2]   School of Materials and Engineering, Jiangsu University of Technology, Changzhou 213001, China; zhubin@jsut.edu.cn

*   Correspondence: toby@nwpu.edu.cn; Tel.: +86-029-8846-0294

Abstract: To investigate the high-cycle fatigue (HCF) behavior of TNM alloys, three different microstructures were designed and obtained by different heat treatments. Staircase tests and fatigue tests in a finite life-region were performed to evaluate the fatigue properties. Then, the fracture surfaces were analyzed to study the fracture behavior of TNM alloys with different microstructures. Results showed that the TNM alloys with duplex microstructure possesses the highest fatigue strength and fatigue life, followed by near lamellar TiAl alloys. HCF failure exhibited cleavage fracture morphologies, and multiple facets were generated in the crack initiation region of different TNM alloys. Two different crack initiation modes, subsurface crack nucleation and surface origin, were observed. Both crack initiation modes appeared in near lamellar alloys, while only subsurface crack initiation were obtained in the duplex (DP) alloy. It contributes to the high scatter of *S-N* data. The HCF failure of TNM alloys was dominated by crack nucleation rather than crack propagation. These findings could provide guidance for optimizing the microstructure and improving the HCF properties of TiAl alloys.

Keywords: titanium aluminides; microstructure; high-cycle fatigue; fracture surface; crack nucleation

1. Introduction

Gamma TiAl-based alloys have been successfully applied in aerospace and automotive industries after decades of developments [1–3]. In recent years, TiAl alloys containing a large amount of β-stabilizing elements, such as Nb and Mo, have attracted much more attentions due to their excellent elevated temperature properties [4–7]. Among them, the TNM alloy, which contains a balanced concentration of Nb and Mo, was recognized as the representative third generation TiAl alloy [8,9]. It has the potential for utilization as the last stage low-pressure turbine blades in advanced geared turbofan engines.

As the most expected and important applications of TiAl alloys, turbine blades and exhaust valves in engines generally serve under cyclic loading conditions [10,11]. Hence, it is important to investigate their fracture behavior during high-cycle fatigue (HCF) for improving the service property of TiAl alloys. Most of the previous researches have been focused on fatigue crack growth [12–15]. It was demonstrated that the low ductility and toughness of TiAl alloys result in a low tolerance to fatigue crack growth and a relatively steep slope of the Paris region [16,17]. Due to the rapid fatigue crack growth rate, the threshold stress intensity has been used for directing component design and predicting the fatigue life of TiAl alloys [18].

Recent studies on fatigue behavior revealed that the crack initiation plays an important role in the fatigue fracture process of high strength steels [19], titanium alloys [20–22] and TiAl alloys [23,24].

Multiple crack initiation modes were observed during the fatigue fracture of those alloys, which may lead to a separation of the fatigue life and increase the difficulty of lifetime prediction [25–28]. It has been illustrated that the fatigue cracks in TiAl alloys could nucleate at lamellae interface, grain boundary and intersection site of slip planes, which revealed a strong correlation between crack nucleation and the microstructure of TiAl alloys [29–31]. Therefore, an in-depth understanding of the crack nucleation, especially its correlation with microstructure, would contribute to the optimization of HCF properties of TiAl alloys. Additionally, more studies were required for systematically investigating the HCF behavior of TiAl alloys with a high β-stabilizing element content.

In this work, TNM alloys with different microstructures were designed and utilized for studying the effect of microstructure on the HCF of TiAl alloys. The fatigue strength was evaluated by staircase tests. The effect of microstructure on the HCF behavior was discussed based on the mechanical results and fractography analysis.

2. Materials and Methods

The TNM alloy investigated in this study was prepared by twice vacuum arc remeltings followed by induction skull melting. The practical composition of the ingot was Ti42.92Al4.01Nb0.99Mo0.18B (at.%), which was measured by inductively-coupled plasma atomic emission spectrometers in the Northwest Institute for Non-Ferrous Metal Research, Xi'an, China. After the measurement of composition, ingot breakdown was accomplished through canned forging. Then, the pancake was hot isostatic pressed (HIP) at 1280 °C and 140 MPa for 4 h. Two-step heat treatments were applied to the HIPed alloy, see Table 1. The different solution-treatments led to different microstructures including duplex (DP) and near lamellar (NL), as shown in Figure 1. The volume fractions of the constituents were determined through quantitative analysis of SEM micrographs, and listed in Table 1. DP alloy contains equiaxed γ (TiAl) grains, B2 phase, and lamellar colonies composed of α_2 (Ti$_3$Al) and γ lamellae. Meanwhile, a lot of γ grains and ω particles precipitated from retained B2 phase during cooling of the TNM alloys. NL#1 alloy was composed of lamellar colonies, as well as γ grains and the B2 phase which discontinuously distributes at colony boundaries. NL#2 alloy was solution-treated at a higher temperature, which resulted in larger lamellar colonies with a massive B2 phase and no γ grains located at colony boundaries.

Table 1. Heat treatment routes and volume fractions of the constituents of three different microstructures.

Microstructure	Heat Treatment	Volume Fractions (%)			Colony Size (μm)
		α_2/γ Colonies	Equiaxed γ	B2	
DP	1230 °C/1 h/AC + 850 °C/6 h/FC	50.5	33.9	15.6	30–40
NL#1	1280 °C/1 h/AC + 850 °C/6 h/FC	91.7	3.2	5.1	45–55
NL#2	1300 °C/1 h/AC + 850 °C/6 h/FC	93.3	0.1	6.6	60–70

Uniaxial tensile fatigue tests were conducted at room temperature for measuring the HCF property of TiAl alloys. The geometry of a diabolo specimen used for fatigue test and the fixed specimen during HCF test are shown in Figure 2. The curvature in the middle of the specimen guarantees strain concentration and failure in the center. Tensile fatigue tests were performed on a QBG-50 HCF machine (Qianbang, Changchun, China). The stress sinusoidally varied between maximum and minimum tensile stress with a stress ratio of 0.1 and a frequency of 150–160 Hz. All the specimens were mechanically ground to reduce the surface roughness. Additionally, uniaxial tensile tests were carried out at room temperature for assessing the tensile properties of TiAl alloys before fatigue tests. The tensile tests were performed on an INSTRON 1195 machine (Instron, Canton, OH, USA) with a strain rate of 0.5 mm/min. Cylindrical specimens with a gauge length of 25 mm and a diameter of 5 mm were used in the tensile tests.
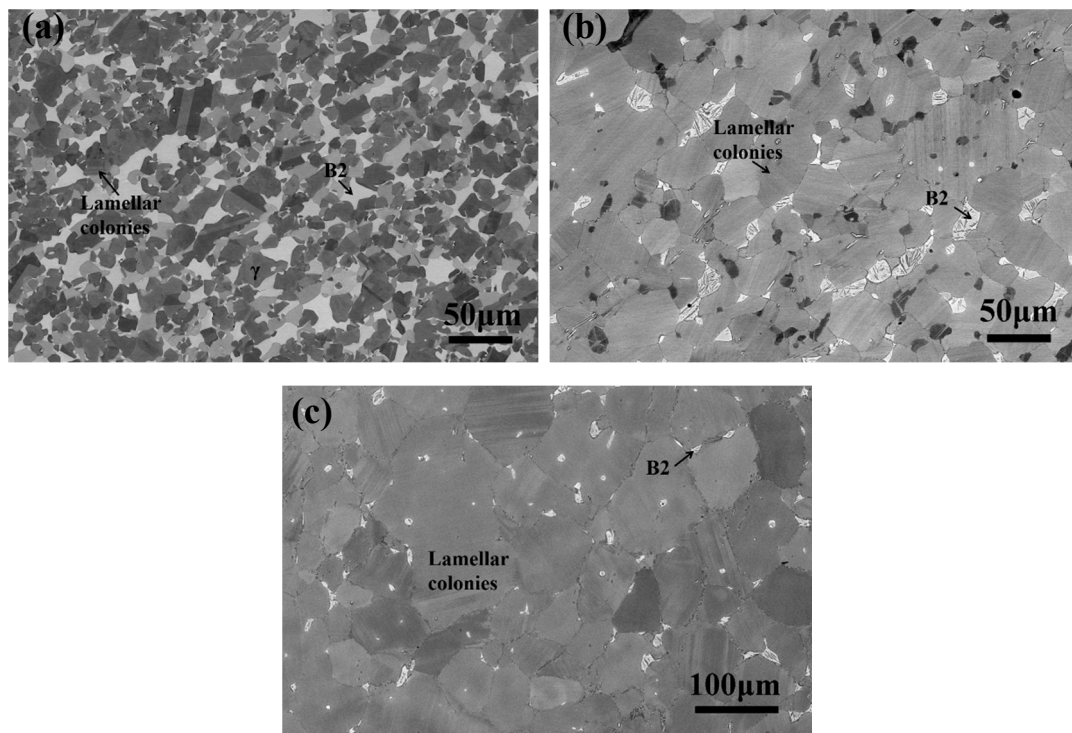
Figure 1. Back scattered electron (BSE) images of TNM alloys with different microstructures: (**a**) DP alloy; (**b**) NL#1 alloy; and (**c**) NL#2 alloy.
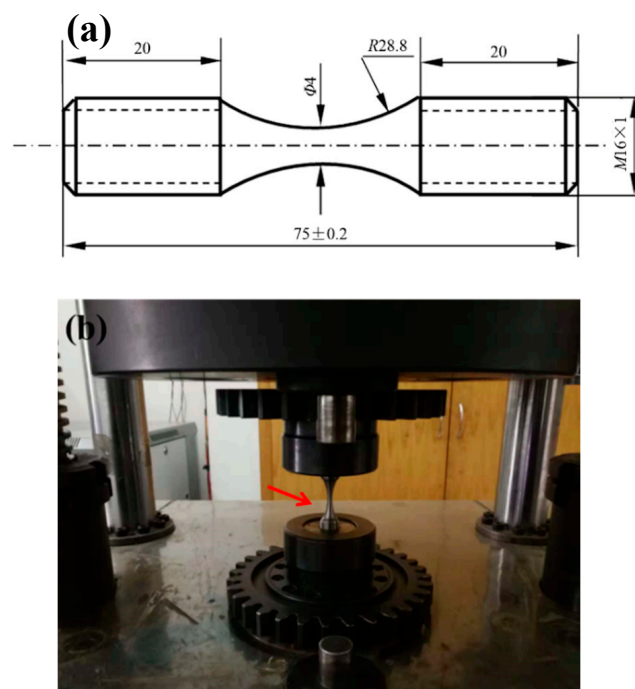

Figure 2. (**a**) Geometry of a diabolo specimen used for the uniaxial tensile fatigue test (dimensions in mm) and (**b**) the fixed fatigue specimen during HCF test.

The microstructure of the raw material and fractured specimens were analyzed by a HITACHI SU3500 scanning electron microscope (SEM, HITACHI, Tokyo, Japan) in the back scattered electron (BSE) mode. The morphology of fatigue fracture surface was characterized using the secondary

electron (SE) mode. The samples used for microstructure characterization were prepared by standard metallographic procedure. The surfaces were mechanically ground and electrochemically polished.

3. Results and Discussion

3.1. Fatigue Properties

3.1.1. Fatigue Strength

The fatigue strengths of TiAl alloys with different microstructures were estimated by staircase methods [32]. As shown in Figure 3a, the ultimate tensile strengthes (UTS) of DP, NL#1 and NL#2 alloys obtained from RT tensile tests were 820 MPa, 890 MPa and 860 MPa, respectively. During the staircase tests, the maximum stress, σ_m, for the first specimen was determined according to the tensile strength. It has been illustrated that the ratio between the fatigue strength and UTS of TiAl alloys was about 0.7–0.8 at RT [33]. Thus, the initial stress levels in staircase tests of all TiAl alloys were determined to be 620 MPa. During staircase tests, the stress level of the subsequent test depended on the result of the prior test. The expected fatigue life of TiAl alloys for this study was defined to be 10^7 cycles. If the specimen failed before reaching 10^7 cycles, the prior test was classified as failure, and the subsequent test would be conducted at a lower stress; otherwise, it is grouped in pass classification, and the next specimen would be tested at a higher stress level. The stress decrement and increment between consecutive stress levels, $\Delta\sigma$, were 20 MPa. The results obtained from staircase tests are shown in Figure 3b–d.
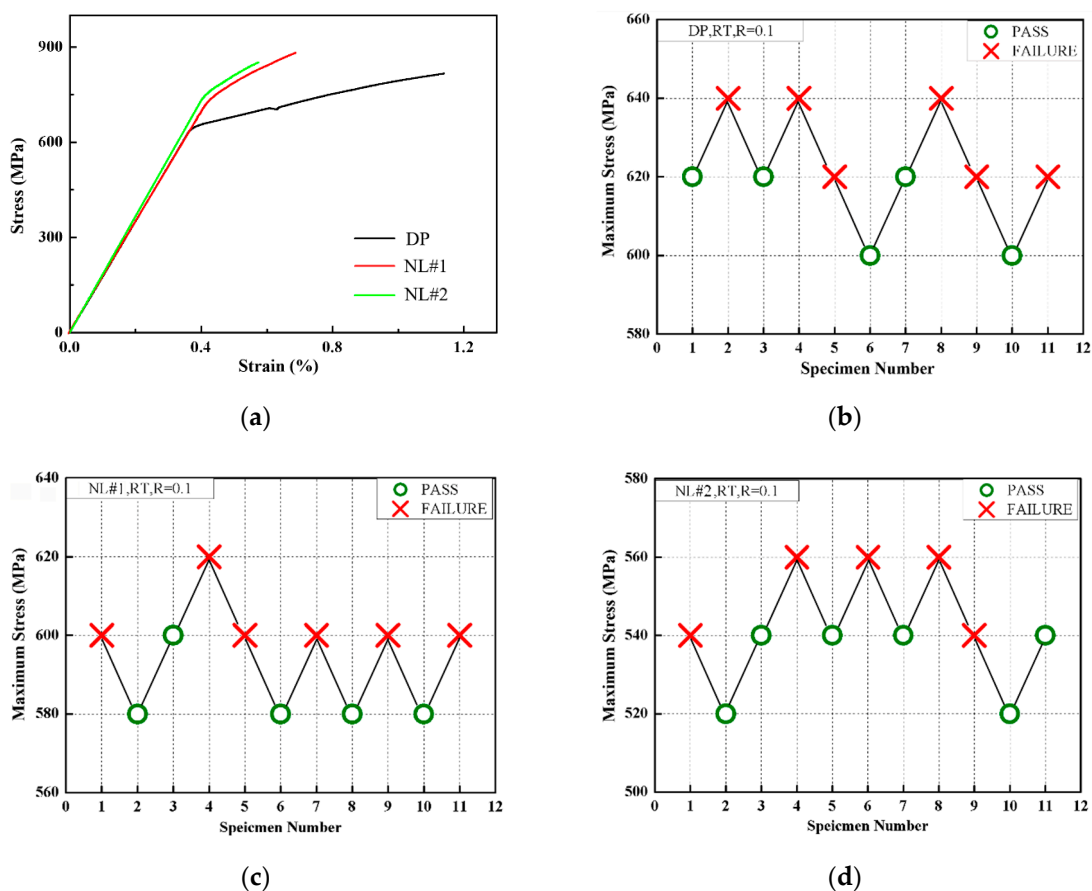

Figure 3. (**a**) Tensile stress-strain curves and Up-and-down diagrams obtained from staircase tests of different microstructural TiAl alloys: (**b**) DP, (**c**) NL#1, and (**d**) NL#2.

As shown in Figure 3b, the maximum stresses are plotted in the ordinate when the specimen number is in the abscissa. The DP specimen at the stress level of 620 MPa passed 10^7 cycles without failure. It was labeled as the first effective specimen. The specimens of both NL#1 and NL#2 TiAl alloys tested at 620 MPa failed before reaching 10^7 cycles. Therefore, the staircase test continued, and the maximum stress decreased until the specimen passed 10^7 cycles. The prior failed specimen was labeled as the first effective specimen and plotted in the up-and-down diagram. As shown in the diagrams of Figure 3, the last specimens were tested at the same stress level with the first effective specimens, which successfully addressed a self-closed condition [34]. The fatigue strength, σ_f, and standard deviation, σ_d, could be calculated by the Dixon-Mood approach [32].

$$\sigma_f = \sigma_0 + \Delta\sigma\left(\frac{A}{C} \pm 0.5\right) \tag{1}$$

$$\sigma_d = \begin{cases} 1.62\Delta\sigma(D+0.029) & D \geq 0.3 \\ 0.53\Delta\sigma & D < 0.3 \end{cases} \tag{2}$$

where σ_0 is the lowest stress of σ_j. σ_j denotes the stress levels corresponding to the less frequent events between pass and failure, which are arranged in ascending sort order. The pass specimens were selected for the calculation of σ_f, and the plus sign was used in Equation (1) for the DP and NL#1 alloys. In contrast, the failure specimens were taken into account, and the minus sign was used for the NL#2 alloy. The parameter D was calculated by

$$D = \frac{BC - A^2}{C^2} \tag{3}$$

The parameters A, B and C were determined by equations

$$A = \sum_{i=1}^{j} i \cdot f_i \tag{4}$$

$$B = \sum_{i=1}^{j} i^2 \cdot f_i \tag{5}$$

$$C = \sum_{i=1}^{j} f_i \tag{6}$$

where n_j was the number of specimens tested at stress level σ_j in the up-and-down diagram, and $j = 0$, 1, 2, ... The results showed that the fatigue strengths of DP, NL#1 and NL#2 alloys were 622 MPa, 594 MPa, and 542 MPa, respectively. Additionally, the standard deviations were all 10.6 MPa for different TiAl alloys. The ratios between the fatigue strength and UTS were separately 0.76, 0.67 and 0.63, which is in consistent with previous investigations.

3.1.2. Fatigue Life

A few more fatigue tests were conducted at high stress levels as supplements. The *S-N* data of different TiAl alloys were obtained and shown in Figure 4. The fatigue life, N_f, were plotted in the abscissa, logarithmic scale. Although the standard deviations of staircase tests were relatively small, the *S-N* relations were quite scattered, especially for the NL#1 alloy. The large scatter of the fatigue life data may be correlated with the damage process of TiAl alloys. The specimens of DP alloy, which failed between 10^6 and 10^7 cycles, had similar maximum stresses and defined a fatigue limit of about 620 MPa. In contrast, the *S-N* data of the NL#1 and NL#2 alloys did not seem to approach such a stress asymptote, which revealed that the failure of NL#1 and NL#2 alloys was resulted from applying enough cycles. It could be deduced from Figure 4 that the DP alloy has the highest fatigue

life, followed by the NL#1 and NL#2 alloys at the same stress level. It verifies the sequence of fatigue strengths illustrated in Section 3.1. However, it has to be noted that, although NL#1 alloy possesses a higher fatigue strength than NL#2 alloy, it's fatigue life at the stress level of 600 MPa is lower. This phenomenon may be related to the large scatter of the *S-N* data. To clarify the problem, the fracture surface was analyzed in the following content for studying the crack initiation, as well as the effect of microstructure on the fatigue properties.
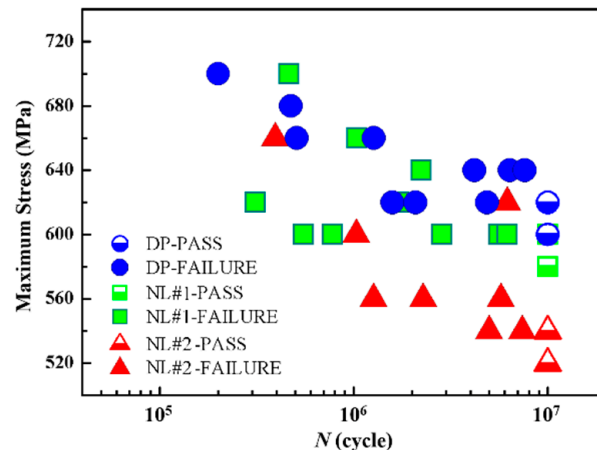

Figure 4. *S-N* data of different TiAl alloys.

3.2. Crack Initiation

The typical fracture surfaces of different TNM alloys tested at various loading conditions were shown in Figure 5. Figure 5a–c presents full views of the fracture surfaces of DP, NL#1 and NL#2 alloys, respectively, as Figure 5d–f shows the corresponding crack initiation sites at higher magnifications. Although the morphology of the crack source is almost the same as that of the crack propagation path for TNM alloys, the crack nucleation sites can still be determined based on the low magnification photographs. It has been illustrated previously that two crack initiation modes: surface crack nucleation and subsurface nucleation, exist during fatigue failure of TiAl alloys [24]. As indicated by black arrows in Figure 5a–c, subsurface crack origins were observed on DP and NL#1 alloys, while the crack originated at the surface of NL#2 alloy.

The fatigue fracture surfaces of all three different TiAl alloys exhibit typical characteristics of cleavage fracture. As shown in Figure 5d, several facets and numerous river patterns can be observed in the crack initiation region of DP alloy. The facets are generated by cleavage fracture on specific planes of γ phases, the size of which corresponds to γ grain size. Since the crack propagation in TiAl alloys may also lead to cleavage facets, and the fatigue crack can initiate in a large area composed of multiple facets [35], only the crack initiation region (rather than the exact crack nucleation position) was identified in the SEM micrographs. The facets were also observed in the crack origin region of NL#1 alloy, see Figure 5e. The sizes of these facets were approximately equal to the colony sizes, which reveals the brittle fracture along α_2/γ interfaces. Apart from these facets, broken lamellar edges and river patterns also appeared on the fracture surface of NL#1 alloy. The morphology of the fatigue fracture surface of NL#2 alloy in the crack initiation region is shown in Figure 5f. The cleavage facets and broken lamellae were similar with NL#1 alloy, except that some facets were distributed along the sample surface, as indicated by black arrows. Therefore, it was classified as surface crack initiation for this sample.
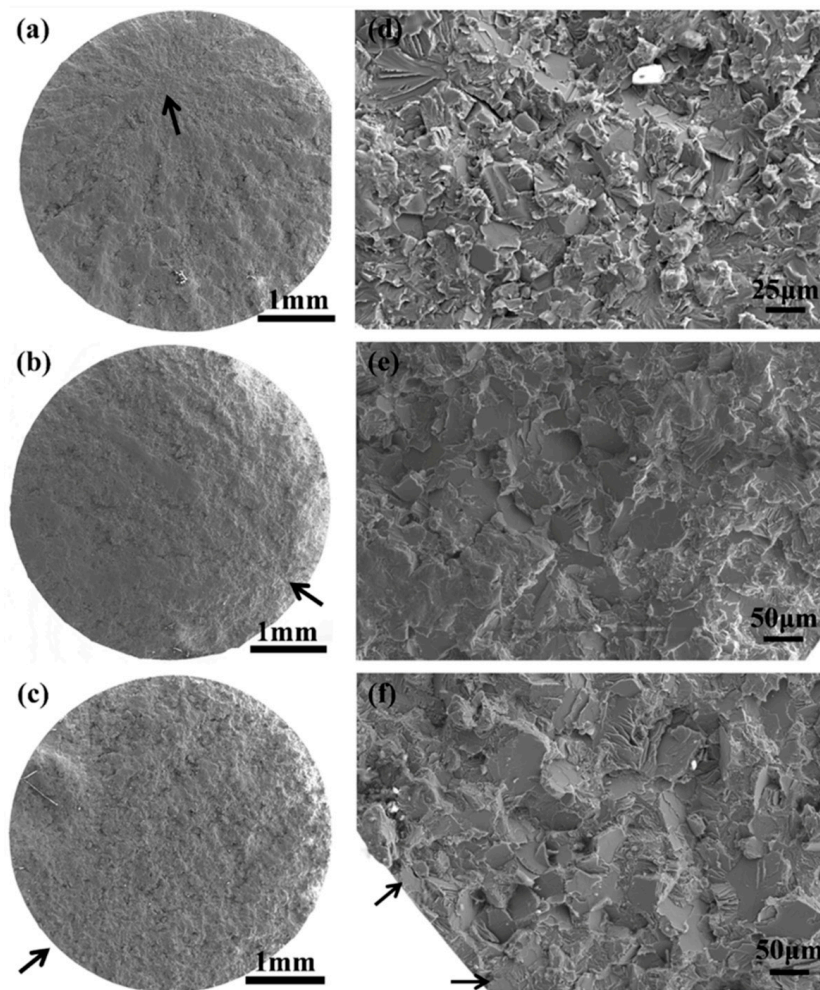
Figure 5. Fracture surfaces of fatigue tested TiAl alloys: (**a**) DP alloy, σ_m = 620 MPa, N_f = 4.9 × 10^6; (**b**) NL#1 alloy, σ_m = 600 MPa, N_f = 5.5 × 10^5; (**c**) NL#2 alloy, σ_m = 560 MPa, N_f = 5.7 × 10^6. (**d**–**f**) show the crack initiation sites at higher magnifications of the DP, NL#1 and NL#2 alloys, respectively.

The surfaces of the fatigue fractured specimens were analyzed. The results were shown in Figure 6. Hollow and solid circles separately represent surface and subsurface crack initiation. As shown in Figure 6, only subsurface crack initiation was observed in the fatigue tests of DP alloy, while both surface and subsurface initiations were obtained for NL#1 and NL#2 alloys. It has been investigated that the existence of two different crack initiation modes may lead to high scattered fatigue results and even duality of *S-N* curves [26,36], which means grouping of the fatigue data into two distinct curves. The scatter of fatigue data of near lamellar TNM alloys is higher compared with that of the DP alloy. It can be attributed to the appearance of surface crack initiation. For NL#1 and NL#2 alloys, it seems that the probability of surface crack nucleation increases with the increasing maximum stress. Nevertheless, no clear and definite correlations between crack initiation mode and fatigue life are observed in this paper.
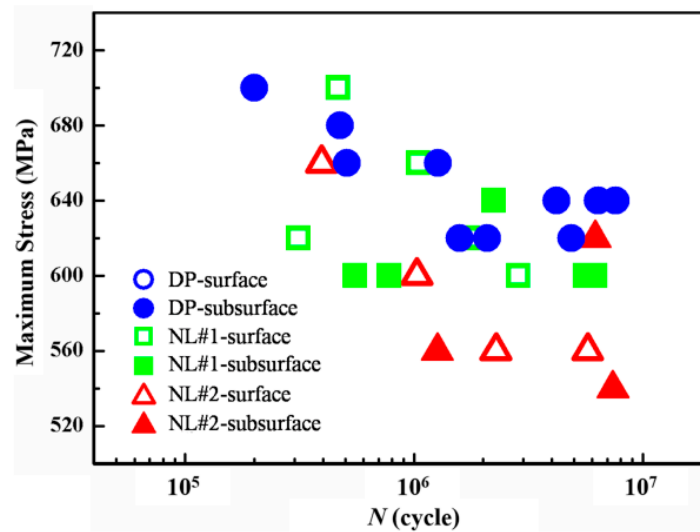
Figure 6. The variation of crack nucleation sites for different TNM alloys in the *S-N* space.

3.3. Effect of Microstructure

The microstructure characteristics and mechanical properties of TNM alloys with different microstructures were listed in Table 2. It can be seen from the table that DP alloy has the highest fatigue strength, σ_f, and tensile fracture strain, ε_t, while NL#1 and NL#2 alloy decreases in turn. The fatigue strength and fracture strain increases with the decreasing colony/grain size. The fracture toughness of TiAl alloys increases with colony size [37]. As confirmed in our former research [38], the duplex alloy possesses a much lower fracture toughness than near lamellar TiAl alloy. The DP alloy thus has weaker resistance to crack growth compared with near lamellar alloys. It has been evidenced by substantial experiments that the fatigue crack growth rate in duplex TiAl alloys is much faster than in lamellar alloys [16,39]. In this study, DP alloy has the highest fatigue strength, and the fatigue strength is negatively correlated with colony/grain size. Therefore, it is reasonable to draw a conclusion that the fatigue fracture of TNM alloys is dominated by microcrack nucleation rather than crack propagation.

Table 2. The microstructure characteristics and mechanical properties of different TNM alloys.

Alloy	Colony/Grain Size (μm)	ε_t (%)	σ_f (MPa)
DP	30–40	1.14	622
NL#1	45–55	0.69	594
NL#2	60–70	0.58	542

As illustrated in Section 3.2, there are two different crack nucleation modes for TNM alloys: surface crack initiation and subsurface initiation. It leads to the large scatter of the fatigue life. Although the correlation between crack nucleation mode and fatigue life can not be determined based on the present data, the results provide valuable implications for optimizing the HCF properties of TiAl alloys. Since the HCF fracture is dominated by crack nucleation, the improvement in HCF properties can be accomplished by decreasing the colony/grain sizes and eliminating the B2 phase, which can reduce stress concentration and modify the deformation heterogeneity according to our previous research [40].

4. Conclusions

The HCF properties of different TNM alloys were obtained by fatigue tests at ambient temperature. The fatigue properties and fracture surfaces were analyzed to investigate the effect of microstructure on fatigue fracture behavior of TiAl alloys. The results are summarized as follows:

(1) The DP alloy possesses the highest fatigue strength, followed by NL#1 and NL#2 alloys. It coincides with the sequence of fatigue life at the same stress level.

(2) Two different crack origin modes were observed: surface crack initiation and subsurface initiation. Both crack initiation modes appeared in near lamellar alloys, while only subsurface crack initiation were obtained in the DP alloy. It contributes to the large scatter of *S-N* data.

(3) Multiple facets were observed in the crack initiation region of all three different TNM alloys, which corresponds to cleavage fracture of γ phase in the DP alloy and along α_2/γ interfaces in near lamellar alloys.

(4) The comparison of fatigue strength agrees well with the colony/grain size among different TNM alloys. It reveals that the crack nucleation plays a more important role than crack propagation in HCF failure of TiAl alloys.

Author Contributions: B.T. conceived and designed the experiments, analyzed the results, wrote and revised the manuscript. B.Z. analyzed the results and wrote the manuscript. W.B. and Y.L. carried out the experiments and discussed the results. J.L. discussed the results and revised the manuscript.

Conflicts of Interest: The authors declare no conflict of interest.

References

1. Yang, R. Advances and challenges of TiAl base alloys. *Acta Metall. Sin.* **2015**, *51*, 129–147.
2. Kim, Y.W. Intermetallic alloys based on gamma titanium aluminide. *JOM* **1989**, *41*, 24–30. [CrossRef]
3. Yamaguchi, M.; Inui, H.; Ito, K. High-temperature structural intermetallics. *Acta Mater.* **2000**, *48*, 307–322. [CrossRef]
4. Clemens, H.; Mayer, S. Design, Processing, Microstructure, Properties, and Applications of Advanced Intermetallic TiAl Alloys. *Adv. Eng. Mater.* **2013**, *15*, 191–215. [CrossRef]
5. Chen, G.L.; Lin, J.P.; Song, X.P.; Wang, Y.L.; Ren, R.R. Development of High Nb Containing High Temperature TiAl Alloys. In *KIM YW, CARNEIRO T. Proceedings of the International Symposium on Niobium for High Temperature Applications*; TMS: Warrendale, PA, USA, 2003.
6. Chu, Y.; Li, J.; Zhu, L.; Liu, Y.; Tang, B.; Kou, H. Microstructure Evolution of a High Nb Containing TiAl Alloy with ($\alpha2 + \gamma$) Microstructure during Elevated Temperature Deformation. *Metals* **2018**, *8*, 916. [CrossRef]
7. Chen, Y.; Cheng, L.; Sun, L.; Lu, Y.; Yang, G.; Kou, H.; Bouzy, E. Characterization of a New Microstructure in a β-Solidifying TiAl Alloy after Air-Cooling from a β Phase Field and Subsequent Tempering. *Metals* **2018**, *8*, 156. [CrossRef]
8. Kim, Y.W.; Kim, S.L. Advances in Gammalloy Materials–Processes–Application Technology: Successes, Dilemmas, and Future. *JOM* **2018**, *70*, 553–560. [CrossRef]
9. Appel, F.; Clemens, H.; Fischer, F.D. Modeling concepts for intermetallic titanium aluminides. *Prog. Mater. Sci.* **2016**, *81*, 55–124. [CrossRef]
10. Loria, E.A. Gamma titanium aluminides as prospective structural materials. *Intermetallics* **2000**, *8*, 1339–1345. [CrossRef]
11. Williams, J.C.; Starke, E.A. Progress in structural materials for aerospace systems. *Acta Mater.* **2003**, *51*, 5775–5799. [CrossRef]
12. Hénaff, G.; Gloanec, A.L. Fatigue properties of TiAl alloys. *Intermetallics* **2005**, *13*, 543–558. [CrossRef]
13. Edwards, T. Recent progress in the high-cycle fatigue behaviour of γ-TiAl alloys. *Mater. Sci. Technol.* **2018**, *34*, 1919–1939. [CrossRef]
14. Appel, F.; Paul, J.D.H.; Oehring, M. *Gamma Titanium Aluminide Alloys—Science and Technology*; John Wiley & Sons: Hoboken, NJ, USA, 2011.
15. Wu, Z.; Hu, R.; Zhang, T.; Zhou, H.; Kou, H.; Li, J. Microstructure determined fracture behavior of a high Nb containing TiAl alloy. *Mater. Sci. Eng. A* **2016**, *666*, 297–304. [CrossRef]

16. Kruzic, J.; Campbell, J.; Ritchie, R. Fatigue-crack propagation in gamma-based titanium aluminide alloys at large and small crack sizes. *MRS Online Proc. Libr. Arch.* **1998**, *552*. [CrossRef]

17. Campbell, J.; Ritchie, R.; Rao, K.V. The effect of microstructure on fracture toughness and fatigue crack growth behavior in γ-titanium aluminide based intermetallics. *Metall. Mater. Trans. A* **1999**, *30*, 563–577. [CrossRef]

18. Rugg, D.; Dixon, M.; Burrows, J. High-temperature application of titanium alloys in gas turbines. Material life cycle opportunities and threats—An industrial perspective. *Mater. High Temp.* **2016**, *33*, 536–541. [CrossRef]

19. Hong, Y.; Lei, Z.; Sun, C.; Zhao, A. Propensities of crack interior initiation and early growth for very-high-cycle fatigue of high strength steels. *Int. J. Fatigue* **2014**, *58*, 144–151. [CrossRef]

20. Jha, S.K.; Szczepanski, C.J.; Golden, P.J.; Porter, W.J., III; John, R. Characterization of fatigue crack-initiation facets in relation to lifetime variability in Ti–6Al–4V. *Int. J. Fatigue* **2012**, *42*, 248–257. [CrossRef]

21. Golden, P.J.; Whitney-Rawls, A.; Jha, S.K.; Porter, W.J., III; Buchanan, D.; Prasad, K.; Chandravanshi, V.; Kumar, V.; John, R. Probabilistic prediction of minimum fatigue life behaviour in α + β titanium alloys. *Fatigue Fract. Eng. Mater. Struct.* **2019**, *42*, 674–685. [CrossRef]

22. Sinha, V.; Pilchak, A.L.; Jha, S.K.; Porter, W.J.; John, R.; Larsen, J.M. Correlating Scatter in Fatigue Life with Fracture Mechanisms in Forged Ti-6242Si Alloy. *Metall. Mater. Trans. A* **2018**, *49*, 1061–1078. [CrossRef]

23. Min, Z.; Xi-Ping, S.; Long, Y.; Hong-Liang, L.; Ze-Hui, J.; Hui-Chen, Y. In situ observation of fatigue crack initiation and propagation behavior of a high-Nb TiAl alloy at 750 °C. *Mater. Sci. Eng. A* **2015**, *622*, 30–36. [CrossRef]

24. Jha, S.; Larsen, J.; Rosenberger, A. The role of competing mechanisms in the fatigue life variability of a nearly fully-lamellar γ-TiAl based alloy. *Acta Mater.* **2005**, *53*, 1293–1304. [CrossRef]

25. Cao, F.; Kumar, P.; Koopman, M.; Lin, C.; Fang, Z.Z.; Chandran, K.R. Understanding competing fatigue mechanisms in powder metallurgy Ti–6Al–4V alloy: Role of crack initiation and duality of fatigue response. *Mater. Sci. Eng. A* **2015**, *630*, 139–145. [CrossRef]

26. Cashman, G.T. A review of Competing Modes fatigue behavior. *Int. J. Fatigue* **2010**, *32*, 492–496. [CrossRef]

27. Pilchak, A.L.; Williams, R.E.A.; Williams, J.C. Crystallography of Fatigue Crack Initiation and Growth in Fully Lamellar Ti–6Al–4V. *Metall. Mater. Trans. A* **2010**, *41*, 106. [CrossRef]

28. Chandran, K.S.R.; Chang, P.; Cashman, G.T. Competing failure modes and complex—Curves in fatigue of structural materials. *Int. J. Fatigue* **2010**, *32*, 482–491. [CrossRef]

29. Bayraktar, E.; Bathias, C.; Hongquian, X.; Hao, T. On the giga cycle fatigue behaviour of two-phase (α2 + γ) TiAl alloy. *Int. J. Fatigue* **2004**, *26*, 1263–1275. [CrossRef]

30. Cottrell, A.H. Theory of brittle fracture in steel and similar metals. *Trans. Met. Soc. AIME* **1958**, *212*, 192–203.

31. Filippini, M.; Beretta, S.; Patriarca, L.; Pasquero, G.; Sabbadini, S. Defect tolerance of a gamma titanium aluminide alloy. *Procedia Eng.* **2011**, *10*, 3677–3682. [CrossRef]

32. Dixon, W.J.; Mood, A.M. A Method for Obtaining and Analyzing Sensitivity Data. *Publ. Am. Stat. Assoc.* **1948**, *43*, 109–126. [CrossRef]

33. Larsen, J.M.; Rosenberger, A.H.; Worth, B.D.; Li, K.; Maxwell, D.C.; Porter, W.J. Assuring reliability of gamma titanium aluminides in long-term service. In Proceedings of the International Symposium on Gamma Titanium Aluminides, San Diego, CA, USA, 28 February–4 March 1999; Minerals, Metals and Materials Society: Warrendale, PA, USA, 1999; pp. 463–472.

34. Gao, Z. *Applied Statistics in Fatigue*; National Defence Industrial Press: Beijing, China, 1986.

35. Jha, S.K.; Szczepanski, C.J.; John, R.; Larsen, J.M. Deformation heterogeneities and their role in life-limiting fatigue failures in a two-phase titanium alloy. *Acta Mater.* **2015**, *82*, 378–395. [CrossRef]

36. Chandran, K.R.; Jha, S. Duality of the *S-N* fatigue curve caused by competing failure modes in a titanium alloy and the role of Poisson defect statistics. *Acta Mater.* **2005**, *53*, 1867–1881. [CrossRef]

37. Chan, K.S.; Kim, Y.-W. Influence of microstructure on crack-tip micromechanics and fracture behaviors of a two-phase TiAl alloy. *Metall. Mater. Trans. A* **1992**, *23*, 1663–1677. [CrossRef]

38. Zhu, B.; Xue, X.; Kou, H.; Li, X.; Li, J. Effect of microstructure on the fracture toughness of multi-phase high Nb-containing TiAl alloys. *Intermetallics* **2018**, *100*, 142–150. [CrossRef]

39. Worth, B.D.; Larsen, J.M.; Balsone, S.J.; Jones, J.W. Mechanisms of ambient temperature fatigue crack growth in Ti-46.5Al-3Nb-2Cr-0.2W. *Metall. Mater. Trans. A* **1997**, *28*, 825–835.

40. Zhu, B.; Xue, X.; Kou, H.; Dong, R.; Li, J. The nucleation of microcracks under tensile stress in multi-phase high Nb-containing TiAl alloys. *Intermetallics* **2019**, *106*, 13–19. [CrossRef]